Anomalous plasma ionization balance induced by 5*s* and 4*f* metastable states

Naoki Kimura,[1,*,†] Priti,[2,*] Naoki Numadate,[3] Ryunosuke Kodama,[4] and Nobuyuki Nakamura[4,2]

[1]*Atomic, Molecular and Optical Physics Laboratory, RIKEN, Saitama 351-0198, Japan*
[2]*National Institute for Fusion Science, Gifu 509-5292, Japan*
[3]*Komaba Institute for Science, The University of Tokyo, Tokyo 153-8902, Japan*
[4]*Institute for Laser Science, The University of Electro-Communications, Tokyo 182-8585, Japan*

(Received 29 September 2022; revised 10 August 2023; accepted 29 August 2023; published 28 September 2023)

Metastable states in an atomic energy-level structure greatly influence atomic processes in plasmas. In particular, high-energy long-lived metastable levels brought about by 5*s* and 4*f* electrons in multiply charged heavy ions often trigger anomalous emission and ionization processes in plasmas. Here, we present a theoretical and experimental study of the ionization processes between the moderate-charge-state barium ions Ba^{8+}, Ba^{9+}, and Ba^{10+} in an electron-beam ion-trap plasma. Indirect ionization processes through 5*s* and 4*f* metastable states in the low-density plasma induce production of higher-charge-state ions at electron energies well below the ionization potential. Remarkably, the observed intensity ratio of an emission line of Ba^{10+} to that of Ba^{9+} decreases with increasing electron energy in a particular energy region, implying there is a characteristic electron energy dependence of each ion abundance. We discuss the experimentally observed characteristic behavior by comparing it with a theoretical simulation based on fine-structure-resolved collisional-radiative modeling with ionization balance.

DOI: 10.1103/PhysRevA.108.032818

I. INTRODUCTION

Detection and control of the charge state of highly charged ions (HCIs) are fundamental for a variety of plasma applications. For instance, an extreme-ultraviolet light source based on a laser-driven plasma [1] should maintain efficient production of the objective charge-state ions in order to maintain prominent emission from the HCIs [2–6]. The population distribution of charge states also provides crucial information for plasma diagnostics because it generally depends on the plasma condition. In fact, the systematic investigation of emission spectra of highly charged tungsten ions for a wide range of charge states has contributed to the development of diagnostic methods for fusion reactor plasmas such as ITER (international thermonuclear experimental reactor) [7]. In addition, multimessenger astrophysical observations initiated by the first detection event of neutron-star mergers [8] recently enhanced the importance of understanding the charge-state distribution of moderate-charge-state heavy ions in low-density plasmas. The opacities of ions in astrophysical plasmas produced by compact-object mergers such as neutron-star–neutron-star and neutron-star–black-hole merging events and their effect on the early kilonovae have been theoretically studied by taking the charge-state distribution into account [9–11].

An electron-beam ion trap (EBIT) [12], essentially consisting of a quasimonochromatic electron beam, is a powerful tool for studying level structures and emissions of HCIs. The upper limit of the charge state of HCIs generated by successive ionization with electron impact in an EBIT plasma depends on the electron energy, with increasing energy yielding higher charge states [13]. This general behavior is advantageous for emission-line assignments since the charge state of the ions can be easily identified by observing the electron energy dependence of line intensities in an EBIT (e.g., [14–19]).

An EBIT is also useful for studying atomic processes in plasmas. Recent experimental studies and their comparison with simulations based on collisional-radiative modeling revealed various characteristic excitation and deexcitation processes caused mainly by long-lived metastable states in specific ions with 5*s* and 4*f* electrons [20–24]. Such long-lived levels were recently applied to demonstrate plasma-assisted laser spectroscopy [25] and Penning-trap mass spectrometry [26]. In several HCIs, ionization processes via metastable states have also been observed by monitoring emission spectra at electron energies well below the threshold for production of the HCIs from the ground state of the preceding lower-charge-state ion [27–33]. Ions with many metastable states have the potential to induce complicated ionization balance due to several indirect ionization pathways. Although multimessenger astronomy highlights the importance of such studies for multiply charged ions of medium-mass elements, detailed studies of the ionization balance including metastable states and their effect on the charge-state distribution have not been performed except for some tungsten ions [33].

Here, we present a study of the ionization balance between Cd-like Ba^{8+}, Ag-like Ba^{9+}, and Pd-like Ba^{10+} to deepen the understanding of indirect ionization processes and their effect on the charge-state distribution in a low-density laboratory

*These authors contributed equally to this work.
†naoki.kimura@riken.jp

plasma brought about by their long-lived metastable levels in $5s$- and $4f$-electron configurations outside of the $4d^{10}$ closed shell. We discuss the ionization balance by comparing the experimental emission spectra of barium ions in a compact electron-beam ion trap [34] and theoretical calculations based on fine-structure-resolved collisional-radiative modeling.

II. THEORETICAL CALCULATIONS

Figure 1 shows the level structures of Ba^{8+} and Ba^{9+}. The level structure of Ba^{10+} was shown in our previous paper [32]. These level structures, their radiative transition probabilities, and cross sections for electron-impact processes were calculated by using wave functions obtained with the relativistic configurational-interaction (RCI) method using the Flexible Atomic Code (FAC, version 1.1.5) [35]. Details of the theoretical calculations are described in Appendix A. The ground states of Ba^{8+} and Ba^{9+} have $5s^2$- and $5s$-electron configurations outside of the $4d^{10}$ closed shell, respectively. Their excited levels are classified as inner-shell excited levels (blue) or outer-shell excited levels (red). Due to the intrinsic property of inner-shell excited levels, their energy levels are relatively high. The outer-shell excited levels are sparsely distributed, reflecting the small number of valence electrons. This sparse level structure with few possible decay channels results in a number of long-lived metastable levels without an $E1$ (electric dipole) transition decay channel. The ground and metastable states that have lifetimes longer than 0.1 ms are denoted by A–E and a–g for Ba^{9+} and Ba^{8+} ions, respectively. The lifetimes and the ionization energies for these levels are calculated with FAC, as listed in Table I. The populations of the metastable levels in each charge state at an EBIT plasma estimated by the collisional-radiative (CR) model are also summarized in Table I. The low-lying $(5s5p_{1/2})_{J=0}$ and $(5s5p_{3/2})_{J=2}$ levels in Ba^{8+} (b and c, respectively) are metastable due to the absence of an $E1$ decay path. The $5s5d$ energy levels in Ba^{8+} are higher than the $5s4f$ configuration, and thus, the $5s4f$ states (d–g) are also long-lived levels without an $E1$ decay path. In Ba^{9+}, the $4f$ states (B and C) can decay to $5p$ levels only through $E2$ (electric quadrupole) transitions. The inner-shell excited fine-structure levels (D and E) are also metastable due to their large total angular momenta, and thus, their populations should be high in an EBIT plasma.

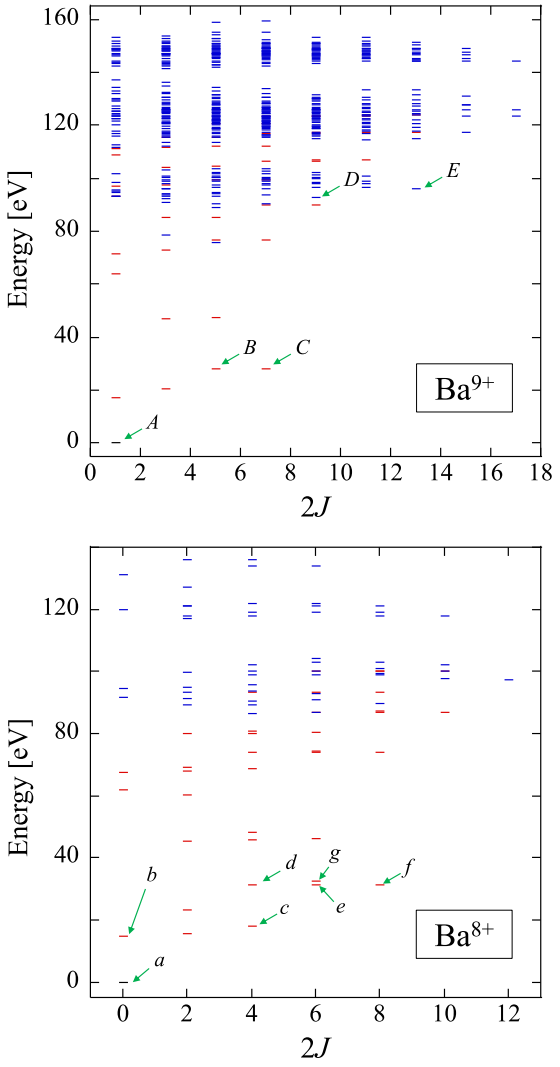

FIG. 1. Energy levels of Ba^{9+} and Ba^{8+} calculated with FAC. The vertical axis is the energy from the ground state for each charge state. The horizontal axis shows twice the total angular momentum. The blue and red levels represent inner-shell excited levels and outer-shell excited levels, respectively. The labels A–E and a–g correspond to labels in Table I.

The population flows between Ba^{8+}, Ba^{9+}, and Ba^{10+} taking the long-lived levels into account are schematically shown in Fig. 2. In this paper, we focus on a discussion of the ionization balance of barium ions for electron energies between 100 and 150 eV. This energy range is high enough to generate Ba^{8+} ions but less than the energy threshold for production of Ba^{11+}. In fact, the previous study [32] provided

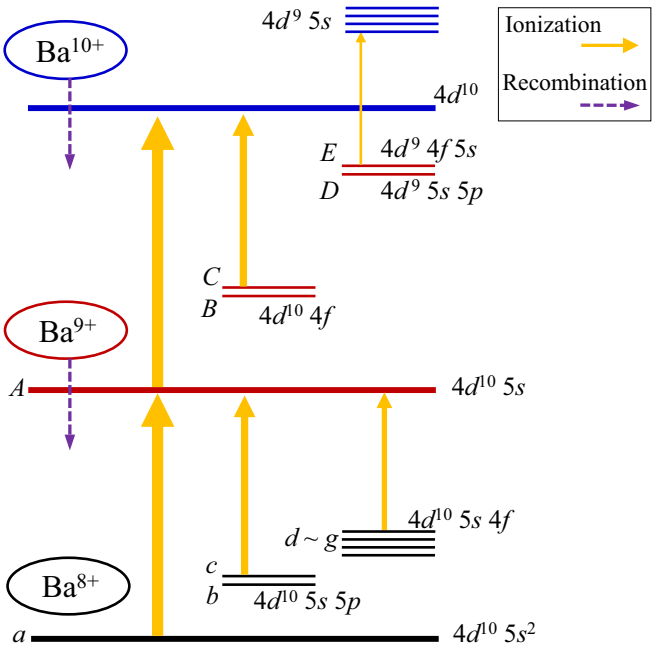

FIG. 2. Schematic overview of the ionization balance from Ba^{8+} to Ba^{10+}. The ionization arrows represent the main pathway from each state.

TABLE I. Summary of the calculated results for the metastable states from FAC. The lifetimes τ are given by the sum of the inverse of the decay rate for all decay channels. ρ is the CR model simulation result for the population in the plasma at an electron density of 10^{10} cm^{-3} and electron-beam energies of 100 and 120 eV for Ba^{8+} and Ba^{9+}, respectively. I_e is the ionization energy for each state. The labels *a*–*g* and *A*–*E* are shown in Fig. 1.

Label	Level	τ (ms)	ρ (%)	I_e (eV)
		Ba^{9+}		
A	$(5s_{1/2})_{J=1/2}$		80.30	145
B	$(4f_{5/2})_{J=5/2}$	3.7×10^{0}	3.12	117
C	$(4f_{7/2})_{J=7/2}$	1.6×10^{1}	10.60	117
D	$[(4d^9_{5/2}\ 5s_{1/2})_3 5p_{3/2}]_{J=9/2}$	1.2×10^{1}	0.39	131[a]
E	$[(4d^9_{5/2}\ 4f_{7/2})_6 5s_{1/2}]_{J=13/2}$	2.7×10^{2}	2.21	127[a]
		Ba^{8+}		
a	$(5s^2)_{J=0}$		78.2	129
b	$(5s_{1/2}\ 5p_{1/2})_{J=0}$		3.36	115
c	$(5s_{1/2}\ 5p_{3/2})_{J=2}$	1.0×10^{1}	12.60	112
d	$(5s_{1/2}\ 4f_{5/2})_{J=2}$	3.8×10^{-1}	0.49	99
e	$(5s_{1/2}\ 4f_{5/2})_{J=3}$	5.0×10^{-1}	0.78	99
f	$(5s_{1/2}\ 4f_{7/2})_{J=4}$	8.8×10^{-1}	1.50	99
g	$(5s_{1/2}\ 4f_{7/2})_{J=3}$	4.3×10^{0}	3.01	98

[a]The ionization energies are calculated by assuming the ionization to $(4d^9_{5/2}\ 5s_{1/2})_{J=3}$.

evidence that Ba^{11+} ions are not generated by electron-beam energies below 150 eV. Therefore, we consider only population transfer between three charge states of barium HCIs (Ba^{8+}, Ba^{9+}, and Ba^{10+}) in the discussion of the ionization balance in the electron energy region studied. The ionization processes from the long-lived metastable levels produce the higher-charge-state ions even at electron energies less than the ionization threshold from the ground state. The collisional ionization rate from the inner-shell excited levels *D* and *E* in Ba^{9+} to the ground state of Ba^{10+} is quite low because these ionization processes require electron exchanges with electron impact. However, the ionization energies from these levels (*D* and *E*) to the excited $4d^9\ 5s$ states in Ba^{10+} are still lower than the ionization potential from the ground state of Ba^{9+}, and these processes may affect the ionization balance. The reduction in charge states due to recombination processes is also included in the ionization balance. The recombination rates are typically $\sim 10^{-2}$ s^{-1}. To effectively produce the higher-charge-state ions, the ionization rate should be larger than the sum of the recombination rates and the rate of charge exchange processes with residual gas. The compact EBIT used in the present study is built into a liquid-nitrogen-cooled ultrahigh-vacuum chamber. The residual gas pressure measured in the room-temperature region of the chamber is typically 10^{-8} Pa. We assume the main component of the residual gas in the trap region is H_2 because of the cryogenic condition. The typical charge exchange process rate between Ba HCIs and H_2 can be estimated to be less than 10^{-2} s^{-1} using the semiempirical Müller-Salzborn formula [36]. This rate is sufficiently slow compared with typical ionization rates (>1 s^{-1} at an electron density of 10^{10} cm^{-1}).

III. EXPERIMENT

To investigate the plasma ionization balance from Cd-like Ba^{8+} to Pd-like Ba^{10+}, we used a compact EBIT [34] providing a well-defined laboratory plasma. The compact EBIT consists essentially of an electron gun, a drift tube (DT), and an electron collector in an ultrahigh-vacuum chamber. The drift tube is composed of three successive cylindrical electrodes (DT1, DT2, and DT3), forming an axial electrical trap potential. The electron beam emitted from the electron gun is accelerated towards the drift tube while being compressed by an axial magnetic field produced by a high-temperature superconducting magnet surrounding the drift tube. The compressed high-density electron beam forms the trap potential in the radial direction and successively ionizes the ions trapped in the drift tube. We define the nominal electron-beam energy for discussions of the energy dependence of the ionization balance as the voltage difference between the cathode and DT2. There is a systematic energy shift between the nominal and real electron energies. The axial potential of the trap region in the EBIT is not a square-well potential, and the voltage applied to DT1 and DT3 affects the trap region. In the present experimental conditions (DT1 = DT3 = 50 V and DT2 = 0 V), the positive leakage potential from DT1 and DT3 at the center of the trap region is +6 V, calculated from the geometry of the electrodes. From the electron-beam parameter, the negative-space-charge potential due to the electron beam can be estimated to be −36 to −30 V in the electron-beam range of 100–150 eV [13]. It is noted the negative-space-charge potential can be reduced by positive space charge due to trapped ions, contributing to the uncertainty of the estimation. The ion number density is less than $\sim 10^7$ cm^{-3} estimated by the maximum number of trapped ions of $\sim 10^5$ and the trap-region size, which was recently measured [37]. The ion number density is three orders lower than the electron density. Thus, the cancellation effect on the negative-space-charge potential is less than 1%; it is negligibly small. Finally, we determined the total systematic energy shift to be approximately −30 to −24 V in the electron-beam range of 100–150 eV. It should be noted that the calculated energy shifts are just analytical estimations. The positive leakage potential is reliable because

the drift-tube geometry is fixed. On the other hand, careful discussion is necessary for determining the absolute value of the negative energy shift due to the space charge. Although we previously reported this estimation of the space-charge shift in the electron-beam energy of around 400 eV to be reasonable [38], we have not verified the estimation procedure for the space-charge potential in the low-energy region (100–150 eV) discussed in the present paper. This estimate indicates that the space-charge shift becomes higher on the lower-energy side due to the increase in the electron density, and a thorough investigation of the space-charge shift in the low-energy electron beam should be done to justify the absolute value. In this paper, we take the estimated shifts only as references, and the above-defined nominal value is adopted for the electron-beam energy hereafter to discuss the relative energy dependence. We also note that the space-charge shift cannot be a positive value even though trapped ions contribute to the positive shift. This is because ions cannot be trapped in the positive-space-charge potential. Therefore, the actual electron-beam energy is definitely smaller than the nominal value plus the leakage potential from the DTs (+6 eV). Barium was introduced as a vapor from an effusion cell [39] operated at 380 °C. In the present paper, we study the electron energy dependence of the charge-state distribution of barium ions in the plasma. The same magnetic field (∼0.05 T) and electron-beam current (∼3 mA) which were suitable for the stable operation in the present energy region were employed throughout the experiments.

The ions produced in the plasma were observed by extreme-ultraviolet (EUV) emission spectroscopy with a wavelength-dispersive spectrometer directly coupled to the EBIT [40]. The wavelength dispersion was performed with an aberration-corrected concave grating with a groove number of 1200 mm^{-1} (Hitachi 001-0660), and the spectra were measured with a Peltier-cooled back-illuminated charge-coupled device (CCD) camera (Roper PIXIS-XO: 400B). The spectral resolution of the EUV measurements was typically 0.03 nm, which was mainly limited by the width of the electron beam regarded as an entrance slit. The wavelength scale was calibrated by using well-known transitions in Kr^{8+} measured beforehand by introducing Kr gas into the EBIT through a gas injector. Details of the reference lines are summarized in the Appendix B.

IV. RESULTS AND DISCUSSION

Figure 3 shows typical experimental EUV spectra for electron energies of 100, 120, and 140 eV along with the

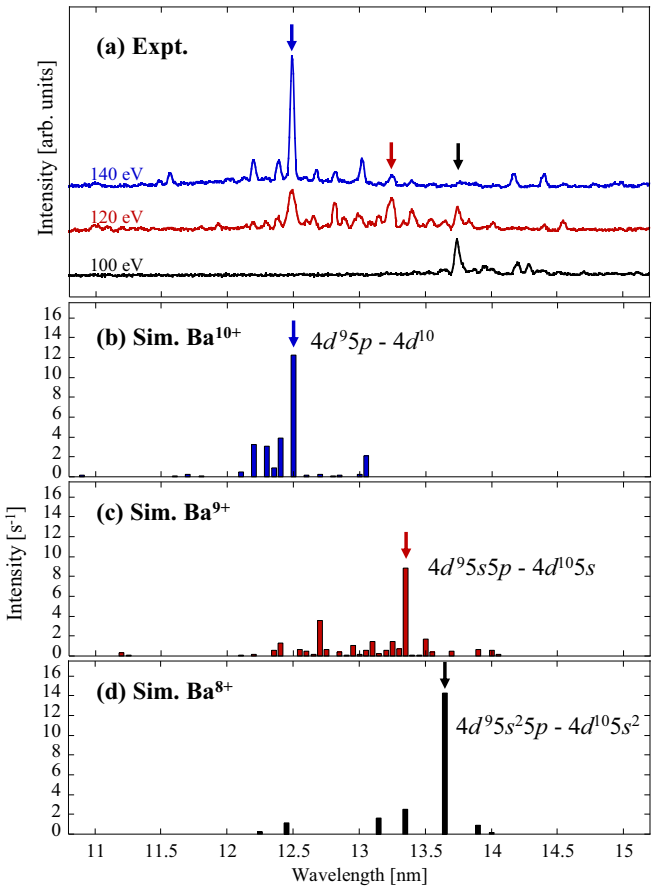

FIG. 3. EUV emission spectra obtained from (a) experiments and (b)–(d) spectral simulations for Ba^{10+}, Ba^{9+}, and Ba^{8+}. The spectral simulations were calculated for an electron energy of 120 eV and an electron-beam density of 10^{10} cm^{-3}. The prominent line positions are denoted with arrows.

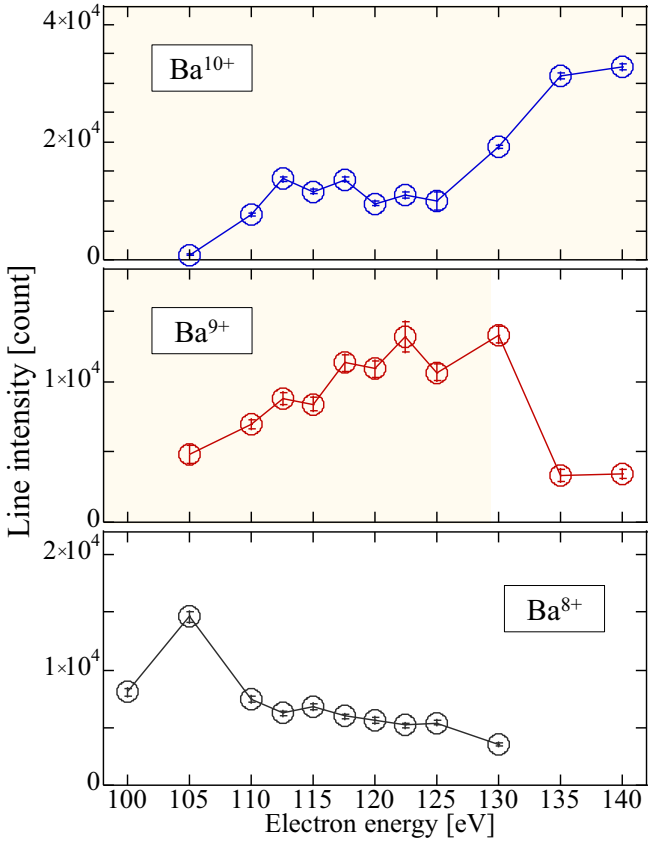

FIG. 4. Electron-beam energy dependence of line intensities of the prominent emission lines denoted in Fig. 3. The experimental electron energy employs the nominal value defined by the voltage difference between the cathode and DT2. The filled yellow area corresponds to the region of electron-beam energy below the ionization threshold from the ground state of the lower charge state.

TABLE II. Summary of the prominent line transitions with their transition wavelengths measured in the present study. The uncertainty of the present measurement is estimated to be 0.02 nm, including systematic error.

				Wavelength in vacuum (nm)	
Color	Ion	Lower level	Upper level	Expt.	Theory
Blue	Ba^{10+}	$(4d^{10})_{J=0}$	$(4d^9_{5/2}5p_{3/2})_{J=1}$	12.51	12.52
Red	Ba^{9+}	$(5s)_{J=1/2}$	$[(4d^9_{3/2}5s_{1/2})_1 5p_{1/2}]_{J=1/2}$	13.25	13.34
Red	Ba^{9+}	$(5s)_{J=1/2}$	$[(4d^9_{5/2}5s_{1/2})_2 5p_{3/2}]_{J=3/2}$	13.27	13.36
Black	Ba^{8+}	$(5s^2)_{J=0}$	$(4d^9_{5/2}5sp_{3/2})_{J=1}$	13.77	13.69

corresponding simulated spectra obtained from CR modeling (see Appendix A). This comparison shows that the experimental spectral features are well reproduced by the simulations. In the wavelength region of 11–15 nm, the observed emissions originate from the $5p$-$4d$ transitions for each charge state. Through a comparison of the experimental spectra with the CR model spectral simulation and previously reported spectroscopic studies [41,42], the prominent lines denoted by arrows in Fig. 3 could be clearly assigned. These lines were then employed to evaluate the ionization balance in the plasma. The emission peaks denoted by the blue, red, and black arrows belong to the $E1$-allowed transitions from $5p$ excited levels to the ground state, as listed in Table II.

Figure 4 shows the electron energy dependence of the line intensities. A linear combination of Gaussian functions was fitted to the prominent lines with the neighbor lines, and the line intensities were analyzed. The error bars represent the fitting errors of the intensity analyses. The Ba^{9+} intensities in Fig. 4 are a sum of two prominent lines because these lines are close to each other. According to the NIST database [43], ionization energies from the ground states of Ba^{8+} and Ba^{9+} are 135.5 and 146.5 eV, respectively. As shown in Fig. 4, the lines of Ag-like Ba^{9+} and Pd-like Ba^{10+} were observed at electron energies much lower than the production thresholds from the ground state of the lower charge states. Even taking into account that the electron-beam energy might be up to 6 eV higher than the nominal energy value due to the leakage potential from the DT electrodes and that the electron beam has an energy width of about 5 eV, such low-energy collisions cannot produce Ba^{10+} and Ba^{9+} only through the ionization processes from the ground states. This implies the existence of indirect ionization processes via metastable

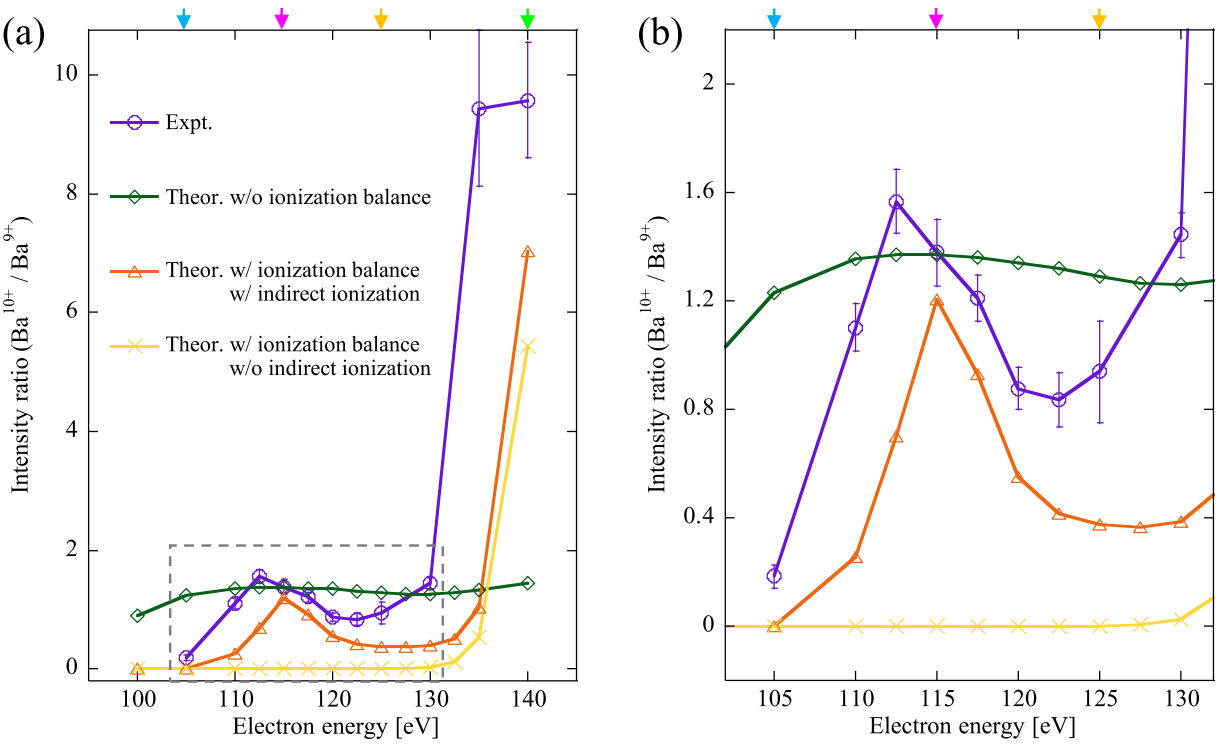

FIG. 5. (a) Electron-beam energy dependence of the intensity ratio between the prominent lines of Ba^{10+} and Ba^{9+}. The experimental error bar corresponds to the fitting error of the objective peaks. The experimental electron energy employs the nominal value defined by the voltage difference between the cathode and DT2. The green lines employ the individual CR model calculation for each ion, which assumes the ion numbers of Ba^{10+} and Ba^{9+} are the same. The orange lines show the full CR-model-calculation results, including the ionization balance. The yellow lines implement the ionization balance but adopt only the ionization from the ground states. (b) Enlarged graph of the region in the dashed rectangle in (a). Colored arrows represent the energies whose ionization balances are described in Fig. 7.

excited levels. Additionally, we note that the emission lines of Ba^{9+} and Ba^{10+} start appearing from the same electron energy (105 eV). This indicates that the effective production threshold for Ba^{10+} is not much higher than that of Ba^{9+}.

For a detailed discussion of the ionization balance from Ba^{8+} to Ba^{10+}, we analyzed the intensity ratio of the emission line of Ba^{10+} at 12.51 nm and the sum of two emission lines of Ba^{9+} at 13.25 nm and at 13.27 nm, as shown in Fig. 5. With this intensity ratio analysis, the fluctuation caused by changes in the number of trapped ions can be excluded. In general, the electron energy dependence of the line ratio from two adjacent ionic states (I_{Z+1}/I_Z, where Z is the charge number) monotonically increases around the ionization threshold. However, as shown in Fig. 5, we experimentally found an anomalous behavior of the line-intensity ratio below 130 eV. The ratio increases below 115 eV, decreases between 115 and 130 eV, and increases again at electron energies larger than 130 eV. To understand this characteristic behavior, we show the theoretical line-intensity ratios obtained from the CR model calculations. Details of the CR model calculation are described in Appendix A. Theoretical transition intensities are given by the product of the relative population n_j of the upper level (j) in the transition, the ion number N_{z+} of the objective charge state $Z+$, and the transition probability A_{ij}. The theoretical line-intensity ratios represented by green lines were independently calculated for each charge-state ion by assuming the same number of Ba^{10+} and Ba^{9+} ions ($N_{10+} = N_{9+}$). These emission lines are from $E1$-allowed $5p$-$4d$ transitions, and thus, their plasma emission properties, defined by the Einstein A coefficients and various population mechanisms for the upper state, are similar. As a result, the CR modeling for individual ions ignoring the ionization balance shows almost no energy dependence in the line ratio. This flat dependence implies that the characteristic electron energy dependence of the experimental line ratio is mainly caused by the difference in the charge-state distribution for each electron-beam energy. In contrast to the green lines, the theoretical calculations including ionization balance (orange lines) qualitatively reproduced the characteristic behavior of the experimental result. The broad peak structure around 115 eV is slightly shifted to higher energy. Although the origin of this systematic shift is not certain at present, calculation uncertainties of theoretical energies of the metastable levels may account for it. The systematic shift between nominal and real electron energies in the experiment may also be a reason. To emphasize the specificity of the experimental behavior, theoretical calculations which implement the ionization balance but exclude the ionization processes from the metastable states are shown in Fig. 5 (yellow lines). Although the low-energy component in the electron beam [full width at half maximum (FWHM) of 5 eV] causes the Ba^{10+} fraction to increase at energies lower than the ionization threshold from the ground state of Ba^{9+} ($I_e = 145$ eV), the increment of the intensity ratio is monotonic. As shown in Fig. 5, the ionization balance that accounts for the indirect ionization processes from metastable states is necessary to reproduce the experimental results.

As mentioned above, the present experimental results combined with the theoretical simulations suggest that the fractional abundances of Ba^{10+} and Ba^{9+} characteristically

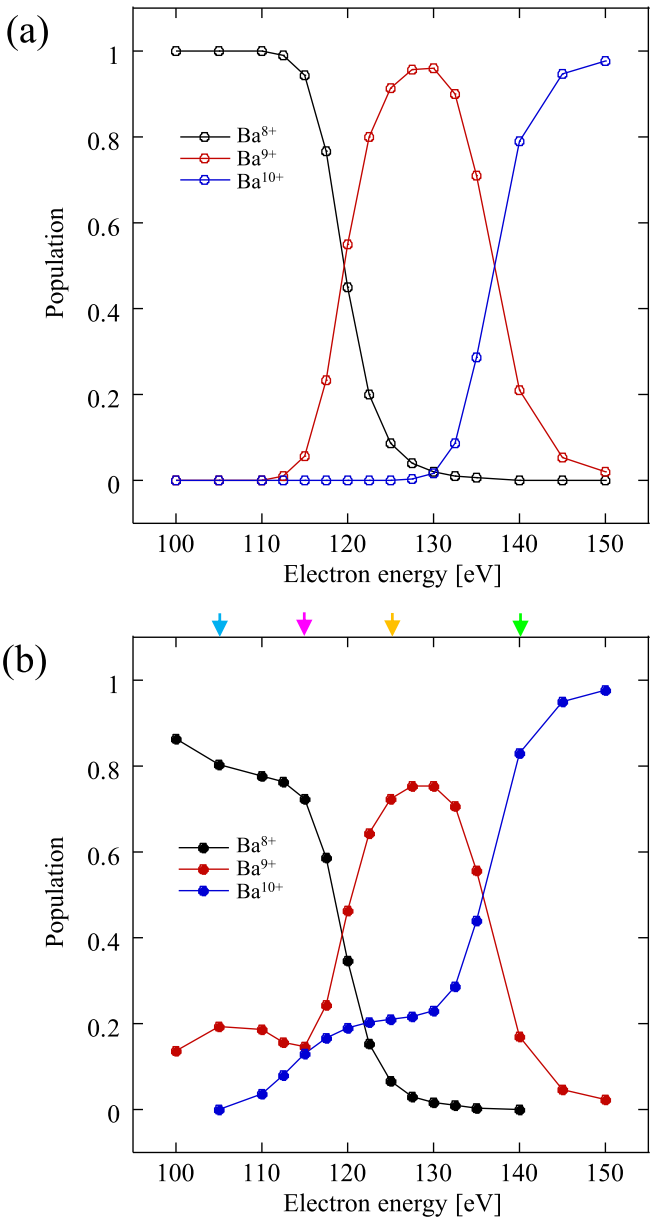

FIG. 6. Simulated fractional abundance for each charge state in the EBIT plasma. (a) The calculation result when the ionization processes from metastable states are not taken into account. (b) The full calculation result including the ionization processes from metastable states. Colored arrows represent the energies whose ionization balances are described in Fig. 7.

change with respect to the electron energy. This electron energy dependence is different from the general behavior, where the ratio of the number of ions between neighboring charge states (higher to lower) monotonically increases with increasing electron energy. In the following, we discuss the origin of the characteristic electron energy dependence of the fractional abundance of these ions. Figure 6 shows the calculation results of the electron-beam energy dependence of fractional abundances of Ba^{8+}, Ba^{9+}, and Ba^{10+} ions in the EBIT plasma. Figure 6(a) represents the calculation results when ionization processes from metastable states are not considered. This shows the valence distribution simply transfers

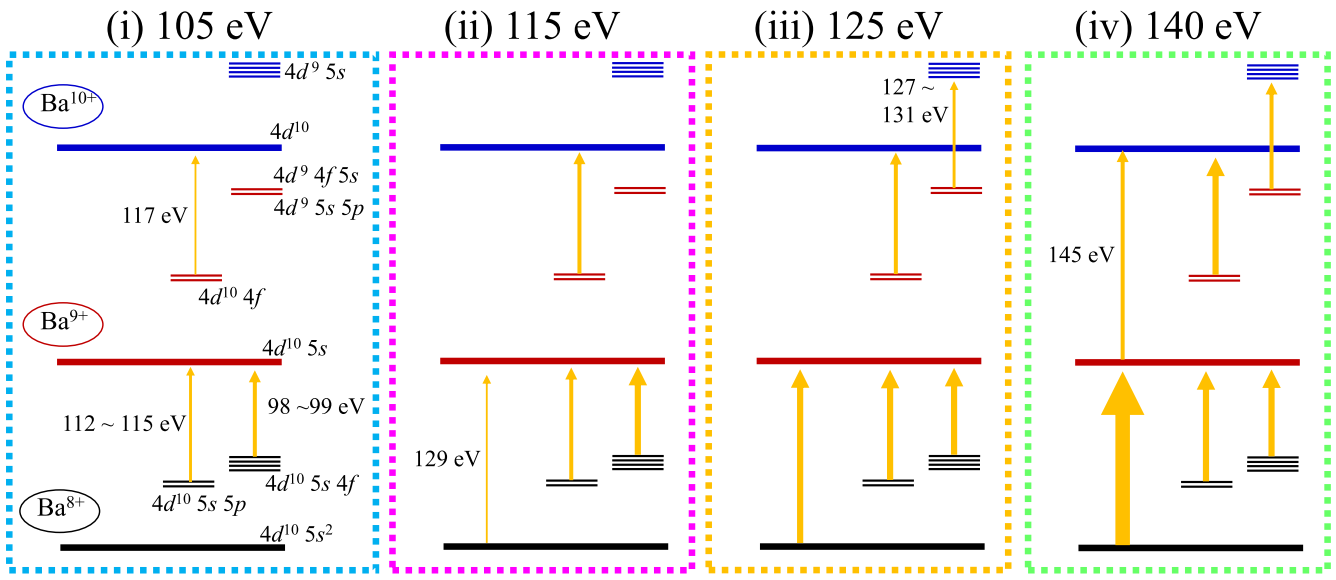

FIG. 7. Schematic ionization processes for electron energies of (i) 105 eV, (ii) 115 eV, (iii) 125 eV, and (iv) 140 eV. In Figs. 5 and 6, the corresponding energies are denoted by colored arrows. The magnitude of the ionization rates for each ionization path is indicated by the size of the arrow.

to the higher charge states with increasing electron energy. In contrast, taking the ionization processes from metastable states induces some remarkable features different from the general behavior, as shown in Fig. 6(b). The fractional abundance of Ba^{9+} has a maximum at around 125–133 eV and a local minimum at 115 eV. The electron energy dependence for Ba^{10+} which appears from 105 eV shows a two-stage increase at 115 and 140 eV.

These characteristic electron energy dependences of the fractional abundance are caused by ionization processes from the metastable states of Ba^{8+} and Ba^{9+}, the mechanism for which can be explained as follows. The possible ionization processes at electron energies of 105, 115, 125, and 140 eV are schematically shown in Fig. 7. At 105 eV, only ionization processes from the $4d^{10}5s4f$ and $4d^{10}5s5p$ metastable states of Ba^{8+} can produce Ba^{9+} ions. The production rate of Ba^{9+} competes with the recombination rate. As a result, the fractional abundance of Ba^{9+} at 105 eV is about 20%. Ionization from $4d^{10}4f$ ($I_e = 117$ eV) can occur due to the finite energy width of the electron beam (FWHM = 5 eV); however, this ionization rate is low (2.2×10^{-4} s^{-1}) because of the low fractional abundance of electrons exceeding the ionization potential. As a result, the Ba^{10+} ions can be generated at 105 eV, but the fractional abundance is still small. At 115 eV, the production rate of Ba^{10+} becomes much faster (1.9×10^{-2} s^{-1}). While the ionization rate from Ba^{8+} to Ba^{9+} also increases, the increase in the Ba^{10+} production process at 115 eV is more effective. As a result, Ba^{10+} shows an initial increase, and the Ba^{9+} population is slightly depleted, which is reflected in the increase in the intensity ratio of Ba^{10+} with respect to Ba^{9+}. At 125-eV electron-beam energy, the ionization path from the ground state of Ba^{8+} is opened so that the population to Ba^{9+} is fully supplied. On the other hand, the Ba^{10+} production rate does not change significantly due to ionization only from metastable states of Ba^{9+}, so the Ba^{10+}/Ba^{9+} intensity ratio decreases. The electron-beam energies above 140 eV have sufficient ionization rates from the Ba^{9+} ground level to Ba^{10+} and produce the secondary increase in the Ba^{10+} population, resulting in the high Ba^{10+}/Ba^{9+} intensity ratio at these energies. As in the above discussion, the precise ionization balance model, taking several ionization processes via metastable states into account, succeeded in qualitatively explaining the characteristic electron energy dependence of the intensity ratio of the plasma emission from Ba^{10+} and Ba^{9+}.

In the above calculation, we assumed that the full width at half maximum of the electron-beam energy is 5 eV from our previous measurement of the electron energy width [38]. Figure 8 shows the electron-beam energy-width dependence

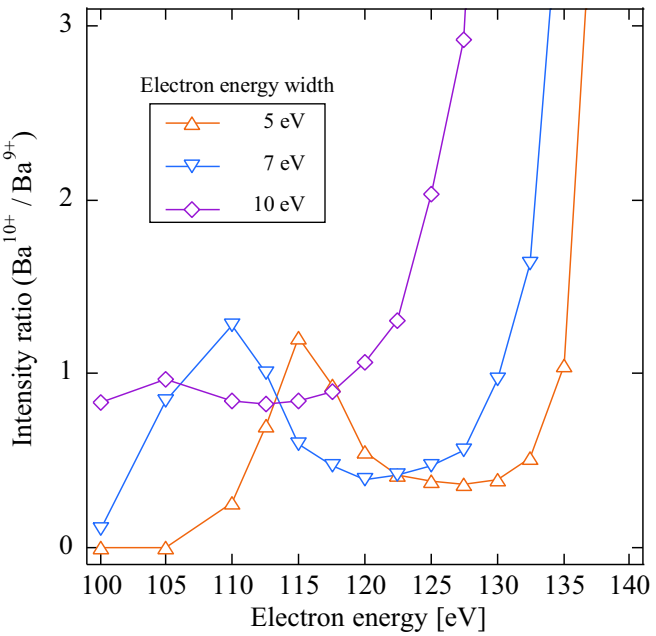

FIG. 8. Electron-energy-width dependence of the theoretical line-intensity ratio of Ba^{10+} and Ba^{9+}.

of the theoretical calculation for the intensity ratio between the prominent lines of Ba^{10+} and Ba^{9+}. As shown in Fig. 8, the characteristic intensity ratio behavior is sensitive to the electron-beam energy width. The broad peak structure in the intensity ratio calculations with the larger electron energy width moves to the low-energy side, and the structure width becomes large. This shift was caused by the increase in the high-energy tail component in the electron energy distribution contributing to the indirect ionization processes. Specifically, the high-energy tail component allows effective ionization from $4d^{10}\ 4f$ of Ba^{9+} even in the energy region below 115 eV, causing the shift of the first increment of Ba^{10+} to the lower-energy side. The ionization from the ground state of Ba^{8+} also arises at lower energies than in the case of the 5-eV energy width, causing a similar shift of the dip position. The high-energy tail component in the electron-beam energy also contributes to various ionization processes other than the assumption in Fig. 7, which broadens the peak structure.

V. CONCLUSION

We experimentally and theoretically investigated the electron energy dependence of the emission line intensities of Ba^{8+}, Ba^{9+}, and Ba^{10+} in an electron-beam ion-trap plasma. The experimental intensity ratio of the Ba^{9+} and Ba^{10+} emission lines showed an anomalous electron energy dependence. The theoretical CR model calculation with ionization balance qualitatively reproduced this behavior. The characteristic ionization balance was explained by taking the contribution of indirect ionization processes via long-lived metastable levels in Ba^{8+} and Ba^{9+} into account. The present demonstration reveals that indirect ionization processes may significantly contribute to the population distribution of heavy ions with $5s$ and $4f$ metastable states. In the present Ba^{8+}–Ba^{10+} case, the complicated metastable states induce a variety of ionization balances during energy increases of only 40 eV from 100 to 140 eV, as shown in Fig. 7, when the quasimonochromatic electron beam with a narrow energy width was employed. The present study suggests that the electron energy in an EBIT plasma cannot be accurately estimated solely by the ion-number ratio between two different charge states for plasma diagnostics of a low-density plasma. In addition, ions with a closed-shell electron configuration and neighbor charge-state ions, such as Ba^{8+}, Ba^{9+}, and Ba^{10+}, generally tend to possess high-energy long-lived levels due to the simple and sparse level structures limiting decay path possibilities. Such ions have the potential to show a characteristic ionization balance reflecting their level structures. Their population is generally high in plasmas because they have high excitation and ionization energies. This enhances the importance of the present knowledge. Furthermore, ionization processes from such metastable states are relevant to research on astrophysical plasmas. In particular, recent simulations of early kilonova emission from neutron-star mergers have implemented the plasma electron temperature dependence of charge-state distributions of medium-mass elements, including Ba^{8+}–Ba^{10+}, for opacity estimation [10]. Deep understanding of the charge-state distribution in a low-density plasma for a wide variety of medium-mass elements, through experimental verification using the well-defined laboratory plasma in an EBIT as demonstrated in this paper, may refine knowledge of opacities in early kilonovae.

ACKNOWLEDGMENTS

We thank Dr. K.C. Chartkunchand (RIKEN) for the critical reading of the manuscript. This work was supported by Japan Society for the Promotion of Science (JSPS) Grants-in-Aid (Grants No. 22K13990 and No. 23K17305) and the RIKEN pioneering projects.

APPENDIX A: THEORETICAL CALCULATION

In the main text, we analyzed the experimental EUV spectra of Ba^{8+}–Ba^{10+} and discussed the characteristic ionization balance in an EBIT plasma from the collisional-radiative (CR) model using FAC [35]. In this Appendix we show the details of the theoretical calculations.

1. Structure and cross-section calculations

We first calculated the level structures, their radiative transition probabilities, and cross sections for electron collisions. Ionic state wave functions for Ba^{8+}, Ba^{9+}, and Ba^{10+} are obtained with the relativistic configurational-interaction (RCI) method, utilizing $4d^{10}5s^2$, $4d^{10}5s^14f^1$, $4d^{10}5s^1nl$ ($n=5$–8, $l=0$–5), $4d^{10}nl^2$ ($n=4,5$, $l=0$–3), $4d^95s^24f^1$, and $4d^95s^25l$ ($l=0$–4) configurations for Ba^{8+}; $4d^{10}5s^1$, $4d^95s^2$, $4d^{10}4f^1$, $4d^{10}nl$ ($n=5$–8, $l=0$–5), $4d^94f^2(5l^2)$ ($l=0$–2), $4d^95s^14f^1$, and $4d^95s^15l$ ($l=0$–3) configurations for Ba^{9+}; and $4p^64d^94f$, $4p^64d^9nl$ ($n=5$–6, $l=0$–3), $4p^54d^{10}4f$, $4p^54d^{10}5l$ ($l=0$–3), $4p^64d^85s^2$, $4p^64d^85p^2$, $4p^64d^85d^2$, and $4p^64d^85s5p$ configurations for Ba^{10+} in addition to the ground states of these ions. The full frequency-dependent Breit interaction in the zero-energy limit for the exchanged photon and higher-order QED effects such as self-energy and vacuum polarization corrections in the screened hydrogenic approximation are also added in a subsequent RCI calculation [35]. Energy levels and transition probabilities of electric-dipole-allowed ($E1$) transitions among all levels, as well as forbidden magnetic dipole ($M1$) and electric and magnetic quadruple ($E2$, $M2$) transitions between the levels generated from a single excitation of valance electrons, were obtained by using the RCI wave functions. The cross sections for electron-impact excitations and ionizations were obtained within the relativistic distorted-wave method using FAC.

2. Collisional-radiative model

The present CR model for Ba^{8+}, Ba^{9+}, and Ba^{10+} takes 297, 378, and 655 excited levels into account, respectively. The considered levels originate from the above-mentioned configurations. The populations of the excited levels are obtained by solving the rate-balance equations for all excited states simultaneously. In the steady state, we assume that these levels are interconnected through only collisional and radiative processes. The present model primarily considered population or depopulation by electron-impact excitation (deexcitation), ionization, and radiative decay and radiative recombination. Other recombination processes such as three-body recombination were ignored due to the low electron density of the EBIT plasma. Dielectronic recombination

processes were not considered because they occur only when the electron-beam energy is equal to the exact energy required for the dielectronic capture condition. Therefore, the rate-balance equation for an excited state j is simply given by

$$\sum_{\substack{i \\ i\neq j}} k_{ij} n_i n_e + \sum_{i>j} A_{ij} n_i + n_+ n_e k_{+j} - \sum_{\substack{i \\ i\neq j}} k_{ji} n_j n_e - \sum_{i<j} A_{ji} n_j - n_j n_e k_{j+} = 0. \quad \text{(A1)}$$

Here, A_{ij}, n_j, and n_e are the transition probability from level i to j, the population of the jth level, and the electron density, respectively. k_{ij}, k_{j+}, and k_{+j}, represent the rate of the electron-impact excitation (deexcitation), the rate of the electron-impact ionization, and the radiative recombination, respectively. Since the EBIT plasma has a quasimonoenergetic electron distribution, all the rates were calculated by integrating the cross sections with a narrow Gaussian electron energy distribution function with a FWHM of 5 eV using FAC. The rate equations for all of the considered levels are solved simultaneously to obtain the level populations.

3. Ionization balance

The intensity of an emission line can be expressed as a product of an upper-level population and its transition probability for an optically thin plasma, i.e., $I_{ji} \propto n_j N_z A_{ij}$. Here, n_j is the relative population of the jth level with respect to the ion population and N_z is the ion number of the objective charge state Z. Therefore, for each ion, relative emission intensities for one charge-state ion are obtained by multiplying the emissivity $n_j A_{ij}$ by the fractional abundance of the ion obtained from the ionization balance. In the ionization equilibrium, for a low-density plasma, populations of the adjacent charge states are coupled by the ionization and recombination processes [44], i.e.,

$$\frac{N_{Z+1}}{N_Z} = \frac{R_I^Z}{R_R^{Z+1}}. \quad \text{(A2)}$$

Here, N_{Z+1} represents the population of the next ionic state from Z. R_I^Z and R_R^{Z+1} are the total ionization and radiative-recombination rates, respectively. In the present study, we consider electron-beam energy at 100–150 eV for the ionization balance of Ba^{8+}–Ba^{10+}. These ions have metastable states which affect the ionization balance, and thus, ionization processes from all of the ground and metastable levels are included by taking the effective ionization and recombination rates as

$$R_I^{Z(\text{eff})} = \sum_i n_i R_{I,i}$$
$$R_R^{Z+1(\text{eff})} = \sum_\nu n_\nu R_{R,\nu}. \quad \text{(A3)}$$

Here, i and ν are the metastable level numbers in the Z and $Z+1$ charge states, respectively. $R_{I,i}$ is the total ionization rate from the ith level, and $R_{R,\nu}$ is the total recombination rate from the νth level. Each fractional abundance of Ba^{8+}–Ba^{10+} was obtained by the combination of Eqs. (A2) and (A3) with the normalization condition $\sum_Z N_Z = 1$.

APPENDIX B: EXPERIMENT: WAVELENGTH CALIBRATION

Table III lists reference transitions to calibrate the wavelength scale of the present emission spectra. We used three electric dipole ($E1$) transitions and two electric quadrupole ($E2$) transitions to the ground $(3d^{10})_{J=0}$ in Kr^{8+} for the wavelength calibration. The transition wave numbers were taken from the level energies in the NIST Atomic Spectra Database level data [43].

TABLE III. List of reference transitions for the wavelength calibration. The wave numbers represent the upper-level energies from the ground $(3d^{10})_{J=0}$ compiled in the NIST database [43]. The corresponding wavelengths are also shown.

Upper level	Transition type	Wave number (cm^{-1})	Wavelength in vacuum (nm)
$(3d^9_{3/2}4p_{3/2})_{J=1}$	$E1$	869958.4	11.4948
$(3d^9_{3/2}4p_{1/2})_{J=1}$	$E1$	864021.1	11.5738
$(3d^9_{5/2}4p_{3/2})_{J=1}$	$E1$	849550.6	11.7709
$(3d^9_{3/2}4s_{1/2})_{J=2}$	$E2$	704514.1	14.1942
$(3d^9_{5/2}4s_{1/2})_{J=2}$	$E2$	693377.1	14.4222

[1] D. L. Matthews, P. L. Hagelstein, M. D. Rosen, M. J. Eckart, N. M. Ceglio, A. U. Hazi, H. Medecki, B. J. MacGowan, J. E. Trebes, B. L. Whitten, E. M. Campbell, C. W. Hatcher, A. M. Hawryluk, R. L. Kauffman, L. D. Pleasance, G. Rambach, J. H. Scofield, G. Stone, and T. A. Weaver, Phys. Rev. Lett. **54**, 110 (1985).

[2] B. Li, T. Otsuka, T. Higashiguchi, N. Yugami, W. Jiang, A. Endo, P. Dunne, and G. O'Sullivan, Appl. Phys. Lett. **101**, 013112 (2012).

[3] T. Wu, T. Higashiguchi, B. Li, Y. Suzuki, G. Arai, T.-H. Dinh, P. Dunne, F. O'Reilly, E. Sokell, and G. O'Sullivan, J. Phys. B **48**, 245007 (2015).

[4] G. O'Sullivan, P. Dunne, T. Higashiguchi, D. Kos, O. Maguire, T. Miyazaki, F. O'Reilly, J. Sheil, E. Sokell, and D. Kilbane, Nucl. Instrum. Methods Phys. Res., Sect. B **408**, 3 (2017).

[5] O. O. Versolato, Plasma Sources Sci. Technol. **28**, 083001 (2019).

[6] F. Torretti, J. Sheil, R. Schupp, M. M. Basko, M. Bayraktar, R. A. Meijer, S. Witte, W. Ubachs, R. Hoekstra, O. O. Versolato, A. J. Neukirch, and J. Colgan, Nat. Commun. **11**, 2334 (2020).

[7] Y. Ralchenko, Plasma Fusion Res. **8**, 2503024 (2013).

[8] B. P. Abbott *et al.* (LIGO Scientific Collaboration and Virgo Collaboration), Phys. Rev. Lett. **119**, 161101 (2017).

[9] M. Tanaka, D. Kato, G. Gaigalas, and K. Kawaguchi, Mon. Not. R. Astron. Soc. **496**, 1369 (2020).

[10] S. Banerjee, M. Tanaka, K. Kawaguchi, D. Kato, and G. Gaigalas, Astrophys. J. **901**, 29 (2020).

[11] S. Banerjee, M. Tanaka, D. Kato, G. Gaigalas, K. Kawaguchi, and N. Domoto, Astrophys. J. **934**, 117 (2022).
[12] R. E. Marrs, M. A. Levine, D. A. Knapp, and J. R. Henderson, Phys. Rev. Lett. **60**, 1715 (1988).
[13] B. M. Penetrante, J. N. Bardsley, D. DeWitt, M. Clark, and D. Schneider, Phys. Rev. A **43**, 4861 (1991).
[14] C. A. Morgan, F. G. Serpa, E. Takács, E. S. Meyer, J. D. Gillaspy, J. Sugar, J. R. Roberts, C. M. Brown, and U. Feldman, Phys. Rev. Lett. **74**, 1716 (1995).
[15] A. Komatsu, J. Sakoda, M. Minoshima, H. A. Sakaue, X.-B. Ding, D. Kato, I. Murakami, F. Koike, and N. Nakamura, Plasma Fusion Res. **7**, 1201158 (2012).
[16] G. V. Brown, P. Beiersdorfer, D. A. Liedahl, K. Widmann, S. M. Kahn, and E. J. Clothiaux, Astrophys. J. Suppl. Ser. **140**, 589 (2002).
[17] J. K. Lepson, P. Beiersdorfer, E. Behar, and S. M. Kahn, Astrophys. J. **590**, 604 (2003).
[18] M. F. Gu, P. Beiersdorfer, G. V. Brown, H. Chen, D. B. Thorn, and S. M. Kahn, Astrophys. J. **657**, 1172 (2007).
[19] K. Fahy, E. Sokell, G. O'Sullivan, A. Aguilar, J. M. Pomeroy, J. N. Tan, and J. D. Gillaspy, Phys. Rev. A **75**, 032520 (2007).
[20] Y. Kobayashi, D. Kato, H. A. Sakaue, I. Murakami, and N. Nakamura, Phys. Rev. A **89**, 010501(R) (2014).
[21] Y. Kobayashi, K. Kubota, K. Omote, A. Komatsu, J. Sakoda, M. Minoshima, D. Kato, J. Li, H. A. Sakaue, I. Murakami, and N. Nakamura, Phys. Rev. A **92**, 022510 (2015).
[22] H. Bekker, O. O. Versolato, A. Windberger, N. S. Oreshkina, R. Schupp, T. M. Baumann, Z. Harman, C. H. Keitel, P. O. Schmidt, and J. Ullrich, J. Phys. B **48**, 144018 (2015).
[23] D. Kato, H. A. Sakaue, I. Murakami, and N. Nakamura, Nucl. Instrum. Methods Phys. Res., Sect. B **408**, 16 (2017).
[24] H. A. Sakaue, D. Kato, I. Murakami, H. Ohashi, and N. Nakamura, Phys. Rev. A **100**, 052515 (2019).
[25] N. Kimura, Priti, Y. Kono, P. Pipatpakorn, K. Soutome, N. Numadate, S. Kuma, T. Azuma, and N. Nakamura, Commun. Phys. **6**, 8 (2023).
[26] R. X. Schüssler *et al.*, Nature (London) **581**, 42 (2020).
[27] J. Sakoda, A. Komatsu, H. Kikuchi, and N. Nakamura, Phys. Scr. **T144**, 014011 (2011).
[28] D. Kilbane, J. D. Gillaspy, Y. Ralchenko, J. Reader, and G. O'Sullivan, Phys. Scr. **T156**, 014012 (2013).
[29] A. Windberger, F. Torretti, A. Borschevsky, A. Ryabtsev, S. Dobrodey, H. Bekker, E. Eliav, U. Kaldor, W. Ubachs, R. Hoekstra, J. R. Crespo López-Urrutia, and O. O. Versolato, Phys. Rev. A **94**, 012506 (2016).
[30] F. Torretti, A. Windberger, A. Ryabtsev, S. Dobrodey, H. Bekker, W. Ubachs, R. Hoekstra, E. V. Kahl, J. C. Berengut, J. R. Crespo López-Urrutia, and O. O. Versolato, Phys. Rev. A **95**, 042503 (2017).
[31] Q. Lu, J. He, H. Tian, M. Li, Y. Yang, K. Yao, C. Chen, J. Xiao, J. G. Li, B. Tu, and Y. Zou, Phys. Rev. A **99**, 042510 (2019).
[32] N. Kimura, R. Kodama, Priti, N. Numadate, K. Suzuki, M. Monobe, and N. Nakamura, Phys. Rev. A **102**, 032807 (2020).
[33] C. L. Yan, Q. Lu, Y. M. Xie, B. L. Li, N. Fu, Y. Zou, C. Chen, and J. Xiao, Phys. Rev. A **105**, 032820 (2022).
[34] N. Nakamura, H. Kikuchi, H. A. Sakaue, and T. Watanabe, Rev. Sci. Instrum. **79**, 063104 (2008).
[35] M. F. Gu, Can. J. Phys. **86**, 675 (2008).
[36] A. Müllar and E. Salzborn, Phys. Lett. A **62**, 391 (1977).
[37] N. Nakamura, N. Numadate, Y. Kono, I. Murakami, D. Kato, H. A. Sakaue, and H. Hara, Astrophys. J. **921**, 115 (2021).
[38] T. Tsuda, E. Shimizu, A. Ali, H. A. Sakaue, D. Kato, I. Murakami, H. Hara, T. Watanabe, and N. Nakamura, Astrophys. J. **851**, 82 (2017).
[39] C. Yamada, K. Nagata, N. Nakamura, S. Ohtani, S. Takahashi, T. Tobiyama, M. Tona, M. Sakurai, A. P. Kavanagh, and F. J. Currell, Rev. Sci. Instrum. **77**, 066110 (2006).
[40] H. Ohashi, J. Yatsurugi, H. A. Sakaue, and N. Nakamura, Rev. Sci. Instrum. **82**, 083103 (2011).
[41] S. S. Churilov and Y. N. Joshi, Phys. Scr. **62**, 282 (2000).
[42] S. S. Churilov, A. N. Ryabtsev, W.-Ü. L. Tchang-Brillet, and J.-F. Wyart, Phys. Scr. **66**, 293 (2002).
[43] A. Kramida, Y. Ralchenko, J. Reader, and NIST ASD Team, NIST Atomic Spectra Database, version 5.7, http://physics.nist.gov/asd.
[44] Dipti, A. Borovik, Jr., R. Silwal, J. M. Dreiling, A. C. Gall, E. Takacs, and Y. Ralchenko, Phys. Rev. A **101**, 032503 (2020).